IEEE Access
Multidisciplinary | Rapid Review | Open Access Journal

SPECIAL SECTION ON DATA-ENABLED INTELLIGENCE FOR DIGITAL HEALTH

Received May 6, 2019, accepted June 3, 2019, date of publication June 20, 2019, date of current version July 10, 2019.

Digital Object Identifier 10.1109/ACCESS.2019.2924041

Effect of Spectral Estimation on Ultrasonic Backscatter Parameters in Measurements of Cancellous Bones

BOYI LI[1], FENG XU[1], CHENGCHENG LIU[2], DAN LI[1], LAWRENCE H. LE[3], DEAN TA[1,4], AND WEIQI WANG[1]

[1]Department of Electronic Engineering, Fudan University, Shanghai 200433, China
[2]Institute of Acoustics, Tongji University, Shanghai 200092, China
[3]Department of Radiology and Diagnostic Imaging, University of Alberta, Edmonton, AB T6G 2B7, Canada
[4]State Key Laboratory of ASIC and System, Fudan University, Shanghai 200433, China

Corresponding authors: Feng Xu (xf@fudan.edu.cn) and Dean Ta (tda@fudan.edu.cn)

This work was supported in part by the National Natural Science Foundation of China under Grant 11525416, Grant 11604054, and Grant 11827808, in part by the International Scientific and Technological Cooperation Project of Shanghai under Grant 17510710700, in part by the Program of Shanghai Academic Research Leader under Grant 19XD1400500, in part by the Shanghai Municipal Science and Technology Major Project under Grant 2017SHZDZX01, and in part by the State Key Laboratory of ASIC and System Project under Grant 2018MS004.

ABSTRACT Objective: the purpose of this paper was to investigate the effect of spectral computation methods on the estimation of the four ultrasonic backscatter parameters, namely, the apparent integrated backscatter (AIB), the zero frequency intercept of apparent backscatter (FIAB), the frequency slope of apparent backscatter (FSAB), and the backscatter spectral centroid shift (SCS) from the backscattered signal of interest (SOI), and their subsequent correlations with cancellous bone parameter [bone volume/total volume (BV/TV)]. Methods: ultrasonic backscatter measurements were performed on 26 bovine cancellous bone specimens using a 1.0-MHz focused transducer. Four spectral estimation algorithms, including the classical periodogram, the autoregressive (AR) Burg algorithm, the AR covariance algorithm, and the AR modified covariance algorithm, were used to calculate the ultrasonic parameters. Influence of the signal's delay time (T1) and its length (T2) on the strength of correlation between BV/TV and backscatter parameters was also studied. Results: the results have demonstrated that the AR-based estimators provide much more reliable and stronger correlations between the BV/TV and backscatter parameters than the classical periodogram. Recommendations for choosing SOI were also suggested. Conclusion: these results indicate that the AR-based method has a promising potential to enhance the performance of evaluation and diagnosis of the cancellous bone using the ultrasonic backscatter method. Significance: the enhancement of the correlation may provide a positive impact on the ultrasonic backscatter method to diagnose and monitor the bone quantity.

INDEX TERMS Ultrasonic backscatter, osteoporosis, cancellous bone, autoregressive spectral estimation.

I. INTRODUCTION

Osteoporosis is a systemic and metabolic skeletal disease [1]–[4]. The disease is characterized primarily by the decrease of bone density and the deterioration of microstructural bone tissue [5], which increases the risk of bone fragility and fracture [6]. It often does not show any symptoms until a fracture occurs [7], causes loss of participation in society, and even disability. Previous studies have predicted osteoporotic fracture in the aged population (50 years and higher) worldwide would be doubled from 158 million in 2010 to 316 million in 2040 [8]. By interpolation, approximately 199 million osteoporotic fracture will be expected in 2019. Osteoporotic fractures frequently occur at the hip, spine, and wrist [9], [10], resulting in chronic pain and even significant disability. Less than half of the patient population who suffer hip fracture can rehabilitate post-injury status [11], [12]. Williamson *et al.* reviewed the costs of fragility hip fractures

The associate editor coordinating the review of this manuscript and approving it for publication was Ying Song.

globally and analyzed 670,173 patients from 27 countries from 1990 to 2015. The costs of health and social care amounted to $43,700 [13] per patient following hip fracture in the first year. The substantial burden fell on patient, family, and society.

Dual-energy X-ray absorptiometry (DXA) and the quantitative computed tomography (QCT) are the major methods to diagnose the bone quality and fracture [14]–[19]. Currently, DXA is considered a clinical gold standard for estimating mineral content in skeleton tissue and fracture risk [20]. However, the bone mineral density (BMD) has been reported to explain only 60-70% correlation with the bone strength [21], prediction fracture risk errors ranging from 20% to 40% [22], and the remaining residuals are believed to associate with other factors such as bone microstructures and elasticity [23]. Thus, measuring BMD alone to evaluate the fracture risk and assess bone status might not be adequate as microarchitecture of cancellous bone also plays an important role. Moreover, because of ionizing radiation, the X-ray based methods may not be desirable for monitoring the condition of bone microarchitecture for infants, pregnant women, and the elderly. Quantitative ultrasound (QUS) [24] has been applied as a noninvasive technique for bone status evaluation with the advantages [25], [26] of non-ionizing radiation, safety, low cost, and portability. The piezo crystal generates the ultrasound wave propagating in bone, the propagation properties are associated with bone properties, i.e., bone densities and microstructures. To address these limitations of the X-ray densitometry, ultrasonic through-transmission techniques have been used to transmit ultrasonic pulses through the cancellous bone to measure the speed of sound (SOS) and the normalized broadband ultrasonic attenuation (nBUA). The multivariate regression analysis of these two parameters has shown them as good indicators for both bone mineral density and mechanical properties [27], [28] in clinical practice. Wear *et al.* [29] have proved the ultrasonic parameters provide complementary information for predicting mechanical properties of cancellous bones.

Recently, ultrasonic backscatter measurement has been demonstrated to be a promising non-invasive technique for evaluating the health status of cancellous bone [30]–[37]. Only one transducer is required for both transmitting and receiving signals. Ultrasound travels into the cancellous bones, interacts with the trabeculae and pores, and is backscattered by the microstructures. Several useful ultrasonic backscatter parameters have been identified, such as the integrated backscatter coefficient (IBC), the broadband ultrasonic backscatter (BUB), and the backscatter spectral centroid shift (SCS). Hoffmeister *et al.* have proposed practical ultrasonic backscatter parameters, namely, the apparent integrated backscatter (AIB) [38], the zero frequency intercept of apparent backscatter (FIAB) [39], the frequency slope of apparent backscatter (FSAB) [40], the normalized mean of the backscatter difference (nMBD) [41], and the normalized backscatter amplitude ratio (nBAR) [42]. These parameters have been investigated using backscatter data from cancellous bones *in vitro* and *in vivo*, and the results have suggested that the ultrasonic backscatter technique is an effective approach [35], [41], [43]–[46]. However, the correlations between bone parameters and ultrasonic parameters (AIB, SCS, FIAB, and FSAB) at 1.0 MHz were found to be weaker than those at 2.25 MHz, 5.0 MHz, and 7.5 MHz for *in vitro* experiments [34], [38], [39]. The estimation of these ultrasonic parameters requires the computation of the power spectrum. While classical spectral estimation is most often used due to its simplicity, it has a poor spectral resolution, leakage, large variance, and instability [47]–[49], which might be an explanation for weaker correlation at 1.0 MHz. To the best of the authors' knowledge, the effect of spectral estimation on the computation of ultrasonic backscatter parameters has not been thoroughly discussed. Further, Liu *et al.* [50] have studied the influence of the starting point or time delay (T1) and the time window (T2) consisting of the backscatter signal on the ultrasonic backscatter parameter estimation and cancellous bone evaluation. They also suggested a procedure to select the signal of interest (SOI) for the AIB, covering the central frequency from 0.5 MHz to 10.0 MHz. However, the selection of SOI for other parameters, such as SCS, FIAB, and FSAB was not fully studied.

The objectives of this *in vitro* study are to investigate the effect of spectral computation algorithms on the estimation of four ultrasonic backscatter parameters (AIB, SCS, FIAB, and FSAB) and to compare the correlation performance between these algorithm-based parameters and the bone volume/total volume fraction (BV/TV). The major innovation of this work is using autoregressive (AR) spectral estimators instead of periodogram to optimize the calculation of ultrasonic backscatter parameters. The effect of the choice of T1, T2 and AR p-order of the backscatter signals on the correlation results are also studied.

II. MATERIALS AND METHODS

A. PREPARATION OF BONE SPECIMENS

Twenty-six fresh cancellous bone specimens were dissected from the heads of bovine femurs, which were purchased in a local slaughterhouse. Operating a computer numerical control band saw with a 0.5 mm thick blade, the cortical bones were stripped along the anatomic orientations of the trabeculae, then the cancellous bones were cut into a cuboid shape. The blade speed was carefully monitored to ensure that the cutting surface was not damaged due to the temperature. A high-pressure oral irrigator was used to remove the marrow out of the medullary cavity. Drying all specimens, and then the dimensions of the specimens were measured by a micrometer (resolution $\pm$ 0.01 mm), and their weights were determined by a precision electronic scale (resolution $\pm$ 0.01 g) as tabulated in Table 1.

B. DATA ACQUISITION

The bone specimens were immersed in distilled water for degasification, then scanned by a Micro-CT Sky-scan1076

TABLE 1. Statistical properties of the specimens.

Parameter	Mean ± SD	Coefficient of Variance
Length (mm)	15.61±4.71	30.18%
Width (mm)	24.47±4.92	20.11%
Height (mm)	20.50±3.11	15.19%
Weight (g)	4.18±2.60	62.29%
Volume (cm^3)	7.77±2.33	30.43%
BV/TV (%)	28.99±11.60	40.00%

scanner (Skyscan, Antwerp, Belgium). The scanning parameters used were 75 kV and 130 μA, with rotating from 0 to 180 degrees at intervals of 0.8 degrees. The data were reconstructed with an 18-μm spatial voxel size, and the BV/TV was measured using the NRecon and CTan software suites (Skyscan, Antwerp, Belgium). Using the Otsu threshold method [51], the threshold for each specimen was automatically designated in histogram analysis. After scanning, the specimens were immersed in the distilled water and degassed again prior to the ultrasonic measurements. Care was taken to ensure specimens do not expose to the air.

The measurements of ultrasonic backscatter signals were performed with the specimens immersed in water as described in [52]. All degassed specimens were placed in a distilled water tank at room temperature (19.0 °C), which was maintained constant by a water heater. A 1.0-MHz ultrasonic transducer with a diameter of 1.90 cm and a focal distance of 2.54 cm (V314, Olympus-Panametrics Inc., MA, USA) was used for the study. The −6 dB frequency band ranged from 0.67 MHz to 1.40 MHz. The transducer was mounted on a three-axis motor controller (Ultrapac scanning, PK268-03B, NJ, USA), placed at 2.54 cm from the surface of the specimens, and connected to an ultrasonic backscatter bone diagnostor (UBBD) [53], which was developed by our Bone Ultrasound Electronic Engineering (BUEE) laboratory in Fudan University. The UBBD had a 50 MHz sampling frequency and 14-bit A/D resolution. The reference signal was an echo from a polished steel plate, placed at the same location of the specimens, ensuring the steel surface reflection had the same travel time as the surface backscatter from the bone samples. The scanning region of interest (ROI) was set at 5.0 mm × 5.0 mm with a scan increment of 0.5 mm. A total of 100 records were obtained with each record being acquired 128 times and averaged to enhance the signal-to-noise ratio.

C. SPECTRAL ESTIMATION ALGORITHMS

Let x[n], $0 \leq n \leq N-1$, be a N-points discrete time series. The periodogram provides the classical power spectral density estimation, namely

$$\hat{P}(\omega) = \frac{1}{N} |X(\omega)|^2. \quad (1)$$

where $X(\omega)$ is the Fourier transform of x[n]. In the AR spectral estimation method, the present value in the time series can be described by the past values. Reference [54] of the process,

$$x[n] = -\sum_{k=1}^{p} a_k x[n-k] + \varepsilon[n]. \quad (2)$$

where p is the AR order, a_k are the AR coefficients, and ε[n] is white noise with variance σ^2. The power spectral density of the AR process is then given by

$$\hat{P}_{AR}(f) = \frac{\sigma^2}{\left|1 + \sum_{k=1}^{P} a_k e^{-(j2\pi kf)}\right|^2}. \quad (3)$$

Different AR estimators have been proposed to determine the AR coefficients and variance. The Appendix provides mathematical details of the three AR estimators we used in this study, which are AR Burg, AR covariance, and AR modified covariance. All the spectral computations were performed in Matlab (Mathworks, Natick, MA).

D. ULTRASONIC BACKSCATTER PARAMETERS

The AIB (dB) [38], [55] is given by

$$AIB = \frac{1}{f_2 - f_1} \int_{f1}^{f_2} 10\, log_{10} \left[\frac{P_{SOI}(f)}{P_{Ref}(f)}\right] df \quad (dB). \quad (4)$$

where the integrand is the backscatter function and the SOI starts at the end of T1 for a length of T2, gated with a rectangular window function. The $P_{SOI}(f)$ and $P_{Ref}(f)$ represent the power spectral density of the signal and the power spectral density of the reference signal, respectively. The limits of integration, f_1 and f_2 correspond to the −6 dB frequency band of the reference signal. The FIAB (dB) is determined by extrapolating to zero-frequency the best fitted line to the backscatter spectrum from f_1 to f_2. The FSAB (dB/MHz) is the slope of the best fitted line. Finally, the backscatter spectral centroid shift [43], [44], SCS (MHz) is

$$SCS = \frac{\int_{f\,min}^{f_{max}} f \cdot P_{SOI}(f) df}{\int_{f\,min}^{f_{max}} P_{SOI}(f) df} - f_0(MHz). \quad (5)$$

where f_{min} and f_{max} are the minimum and maximum values of the transducer's bandwidth, and f_0 is the central frequency of the transducer.

The computation was performed by an i5-6300HQ 2.9 GHz desktop computer with 16 GB RAM. We used the time to compute the four periodogram-based ultrasonic backscatter parameters as a benchmark (i.e., 1384 sec as 1.00 T) and normalized the other computation times by the benchmark for comparison purpose.

E. STATISTICAL ANALYSIS

Pearson's correlation coefficients R and the standard deviation were calculated and analyzed for investigating the linear correlations between BV/TV and ultrasonic backscatter parameters. One-way ANOVA test was also used to assess the potential difference between algorithms. The result was considered statistically significant for the p-values less than 0.05 unless otherwise specified. All statistical computations were processed by IBM SPSS Statistics (IBM Corporation, Armonk, New York, USA).

III. RESULTS

Kolmogorov Smirnov (K-S) normality test was used. The results show that BV/TV and measured ultrasonic backscatter parameters obey the normal distribution at level 0.05.

Fig. 1-4. show the Pearson's coefficients R-value between BV/TV and the four ultrasonic parameters for the four spectral estimators. The resolution of the figures is 0.5 μs$\times$0.5 μs, each pixel included 26 data pairs for calculating correlation R. Following [50], we chose a backscatter signal when the absolute value reached a 5% threshold of the maximum of the signal envelope as the start point of T1. Then we selected the ranges 0-10.0 μs and 1.0-10.0 μs for respective T1 and T2 for the analysis.

When T1 is less than 1.5 μs, and T2 is within 3.0-10.0 μs (Fig. 1.), the AIB has the strong positive correlation with BV/TV with the largest R-values being 0.89, 0.91, 0.90, and 0.92 for AIB_p, AIB_{Burg}, AIB_{cov}, and AIB_{mcov} respectively (Table 2). As T1 extends beyond 2.0 μs for AIB_{cov} and 4.0 μs for the other three methods, the correlation becomes negative. A moderate negative correlation ($R = -0.35$ to -0.64) can be obtained for T1 greater than 4.0 μs. The correlation fluctuates for T2 $< 3.0\,\mu$s. Beyond 3.0 μs, the correlation became steady.

Unlike AIB, SCS correlated with BV/TV negatively (Fig. 2.). Strong negative correlations occur when T1 lies over 6.5 μs and T2 over 7.0 μs in Fig. 2(b) and (c). When T1 lies over 7.0 μs and T2 over 7.0 μs, strong negative correlations occur in Fig. 2(d). With the R-values being -0.84, -0.87, and -0.81 for SCS_{Burg}, SCS_{cov}, and SCS_{mcov}, respectively. However, the only moderate negative correlation of -0.78 was achieved between SCS_p and BV/TV.

FIAB has positive correlations with BV/TV for T1 $<$ 1.0μs and T2 $>$ 3.0μs (Fig. 3.). The maximum achievable R-values are 0.88, 0.89, and 0.88 for $FIAB_{Burg}$, $FIAB_{cov}$, and $FIAB_{mcov}$ respectively, while the moderate positive correlation of 0.71 was obtained for $FIAB_p$.

FSAB presents a negative correlation with BV/TV for T1 $>$ 4.0μs and T2 $>$ 4.0μs with the strongest correlation being -0.84, -0.85, and -0.83 for $FSAB_{Burg}$, $FSAB_{cov}$, and $FSAB_{mcov}$ respectively (Fig. 4.). However, $FSAB_p$ has a moderate correlation of -0.67 with BV/TV.

One-way ANOVA test was also performed between periodogram and other AR-methods to investigate the significant difference between the algorithms. Table 2. provides a summary of the correlation extrema with the 95% confidence interval and the ANOVA test results with the power test.

Selecting two ranges of SOI (T1 $= 0 - 1.0\mu$s, T2 $= 2.0 - 10.0\mu$s for calculating AIB and FIAB, and T1 $= 6.0 - 10.0\mu$s, T2 $= 7.0 - 10.0\mu$s for calculating SCS and FSAB) and the p-order for 17 and 18, the average of Pearson's coefficients with the standard deviation were reported in Table 3.

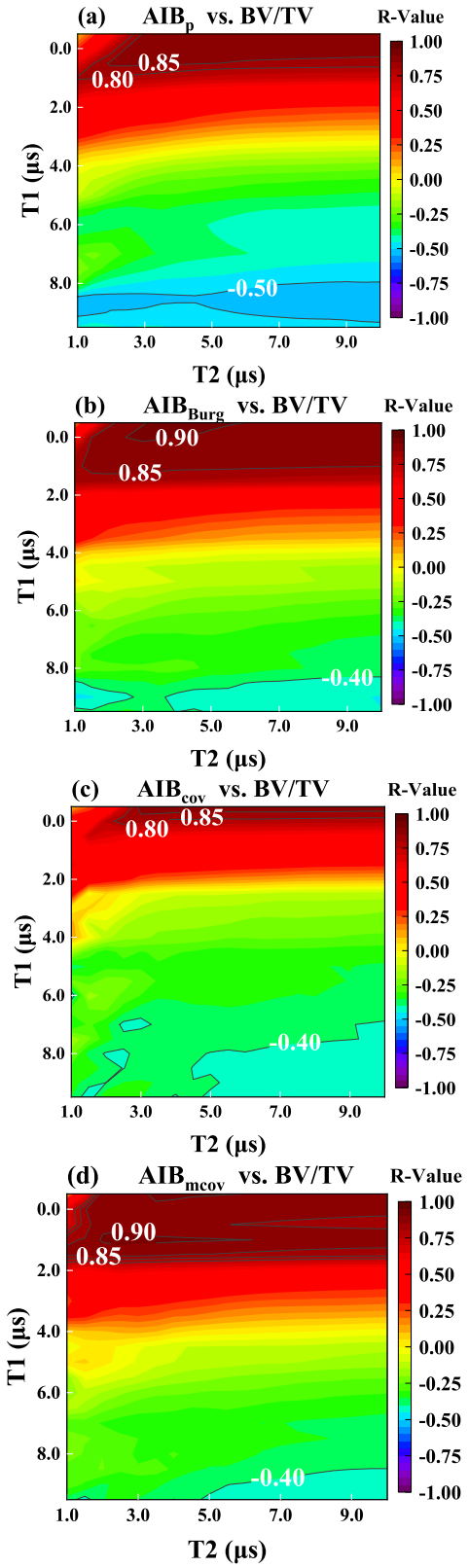

FIGURE 1. Effect of the spectral estimation on the correlation between AIB and BV/TV for 1.0 MHz with AIB calculated by four different methods: (a) Periodogram, (b) AR Burg, (c) AR covariance, and (d) AR modified covariance.

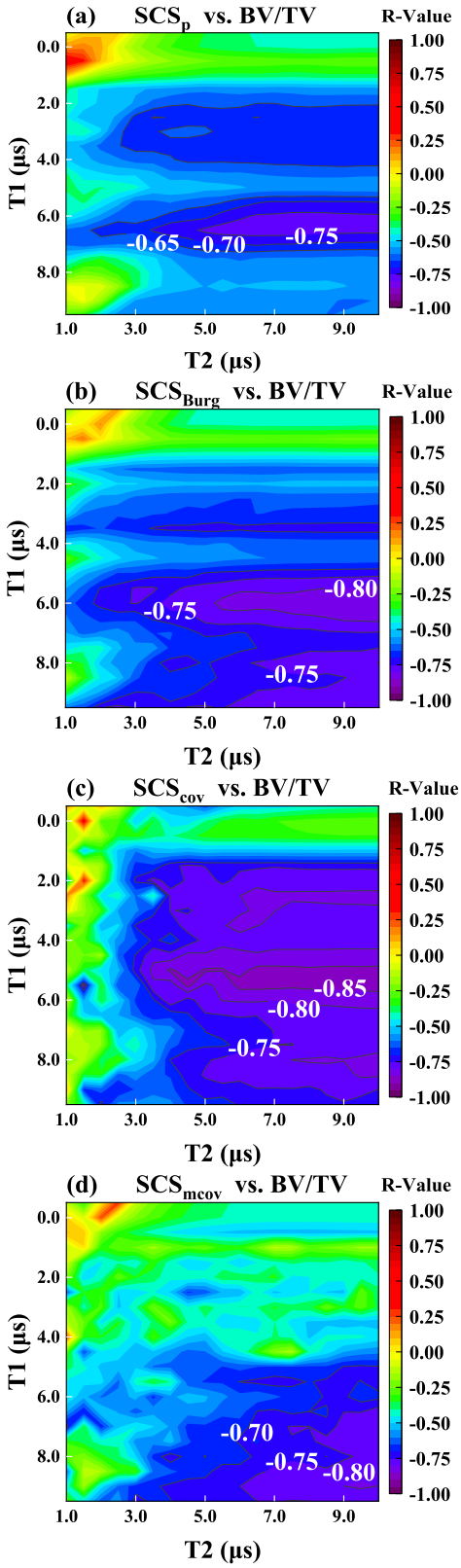

FIGURE 2. Effect of the spectral estimation on the correlation between SCS and BV/TV for 1.0 MHz with SCS calculated by four different methods: (a) Periodogram, (b) AR Burg, (c) AR covariance, and (d) AR modified covariance.

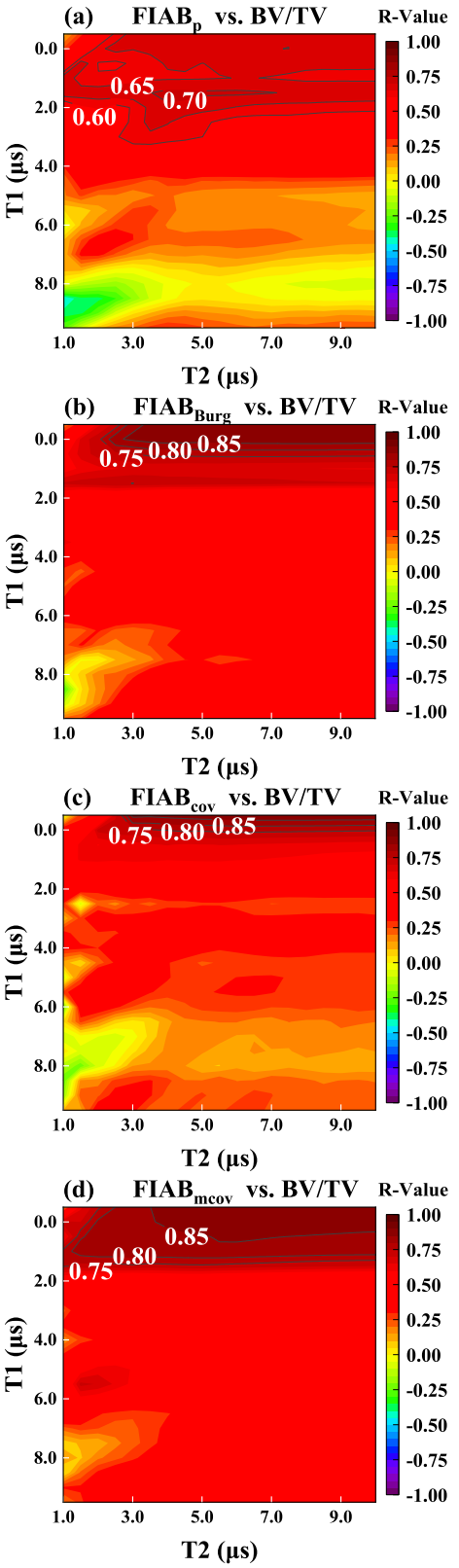

FIGURE 3. Effect of the spectral estimation on the correlation between FIAB and BV/TV for 1.0 MHz with FIAB calculated by four different methods: (a) Periodogram, (b) AR Burg, (c) AR covariance, and (d) AR modified covariance.

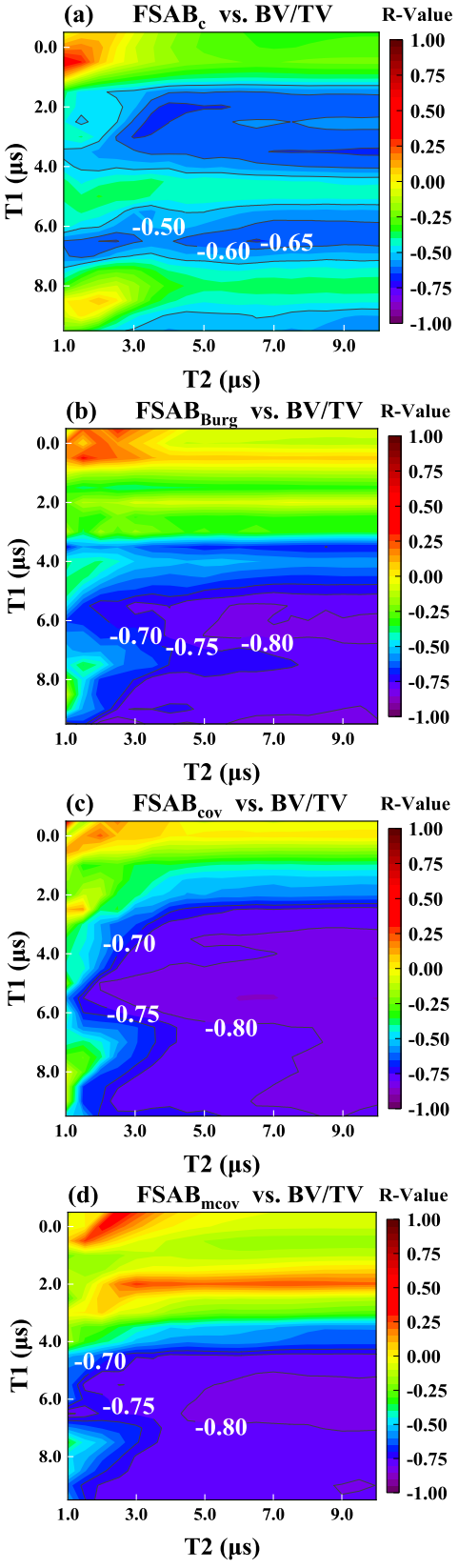

FIGURE 4. Effect of the spectral estimation on the correlation between FSAB and BV/TV for 1.0 MHz with FSAB calculated by four different methods: (a) Periodogram, (b) AR Burg, (c) AR covariance, and (d) AR modified covariance.

TABLE 2. Pearson's correlation coefficients and the ANOVA multiple comparisons.

Comparing Parameters	Algorithms	Pearson's Correlation Coefficients	95% Confidence Interval	
			Lower Bound	Upper Bound
AIB with BV/TV	Periodogram	+0.89**±0.05	+0.75	+0.94
	AR Burg	+0.91**‡±0.04	+0.80	+0.96
	AR cov	+0.90**‡±0.05	+0.77	+0.96
	AR mcov	+0.92**‡±0.04	+0.82	+0.97
SCS with BV/TV	Periodogram	-0.78**±0.07	-0.88	-0.59
	AR Burg	-0.84**‡±0.06	-0.92	-0.70
	AR cov	-0.87**‡±0.04	-0.93	-0.77
	AR mcov	-0.81**‡±0.07	-0.91	-0.65
FIAB with BV/TV	Periodogram	+0.71**±0.08	+0.53	+0.85
	AR Burg	+0.88**‡±0.06	+0.73	+0.95
	AR cov	+0.89**‡±0.06	+0.74	+0.96
	AR mcov	+0.88**‡±0.06	+0.73	+0.95
FSAB with BV/TV	Periodogram	-0.67**±0.06	-0.81	-0.55
	AR Burg	-0.84**‡±0.05	-0.92	-0.73
	AR cov	-0.85**‡±0.05	-0.93	-0.74
	AR mcov	-0.83**‡±0.06	-0.92	-0.67

**. The correlation is statistically significant at the 0.01 level with 2-tails.
†. The estimator is statistically different from the periodogram at the 0.05 level based on one-way ANOVA test.
‡. The estimator is statistically different from the periodogram at the 0.01 level based on one-way ANOVA test.

TABLE 3. The average of Pearson's coefficients with the standard deviation for two different ranges of (T1, T2) values.

Algorithms	p-order	AIB with BV/TV	FIAB with BV/TV	SCS with BV/TV	FSAB with BV/TV
		T1 ≤ 1.0 μs, T2 ≥ 2.0 μs		T1 ≥ 6.0 μs, T2 ≥ 7.0 μs	
Periodogram	-	+0.86**±0.06	+0.68**±0.04	-0.65**±0.08	-0.52**±0.09
AR Burg	17	+0.89**±0.01	+0.82**±0.03	-0.77**±0.01	-0.79**±0.01
	18	+0.89**±0.01	+0.86**±0.05	-0.78**±0.03	-0.79**±0.02
AR cov	17	+0.75**±0.06	+0.76**±0.05	-0.79**±0.01	-0.81**±0.01
	18	+0.82**±0.10	+0.80**±0.11	-0.78**±0.04	-0.81**±0.02
AR mcov	17	+0.88**±0.01	+0.85**±0.02	-0.75**±0.02	-0.79**±0.01
	18	+0.89**±0.02	+0.86**±0.03	-0.74**±0.04	-0.80**±0.02

**. The correlation is statistically significant at the 0.01 level with 2-tails.

Finally, the normalized computation time for the AR Burg, AR cov, and AR mcov algorithms were approximately 3.45T, 4.38T, and 5.59T, respectively.

IV. DISCUSSION

A. COMPARISON WITH PREVIOUS STUDIES AND THE CHOICE OF SOI

The SOI selection directly influences the backscatter parameters for the measurement of cancellous bone. The delay

time, T1 for the backscatter signal should be chosen carefully. A small T1 will include the primary specular echo from the bone surface, which causes the evaluation of the backscatter parameters ambiguous. A large T1 will increase the dominance of the attenuation mechanism over the backscatter. However, the choice of T1 does depend on the central frequency used [50]. In our study, T1 can be large as well for SCS and FSAB. While T1 represents the excluded trabecular volume, T2 denotes the investigated trabecular volume. Backscatter signal comes after the primary echo from the bone surface. A sufficient long T2 will cover the backscatter and the multiple backscatters between trabeculae.

The present study obtained a positive correlation of 0.88 between AIB_p and BV/TV, which is quite close to the correlation 0.78 previously reported [34] using periodogram for the same central frequency of 1.0 MHz. In our study, the AR-based AIB had a slightly stronger association with BV/TV ($R = 0.90 - 0.92$) than the AIB_p ($R = 0.89$).

The SCS_p has a negative correlation with BV/TV, consistent with the result from a previous study [44] using periodogram at 10.0 MHz. Similar to AIB, the AR-based SCS have a much stronger association with BV/TV. In this study, the SCS's correlation values with BV/TV are more negative ($R_{Burg} = -0.84$, $R_{cov} = -0.87$, $R_{mcov} = -0.81$) than the SCS_p's ($R = -0.78$). The power spectrum curve had less variance making the spectrum centroid shift more precise and stable when using AR spectral estimation algorithm. The correlation coefficients of SCS_{mcov} was slightly less than SCS_{Burg} and SCS_{cov}, which might be due to the fact that the AR modified covariance method is more sensitive to noise [47], [56]. Based on Fig. 2(b)-(d)., we suggest $T1 = 7.0 - 10.0\ \mu s$ and $T2 = 7.0 - 10.0\ \mu s$ for the SOI for calculating SCS.

$FIAB_p$ correlates positively with BV/TV ($R = 0.71$) while $FSAB_p$ correlates negatively with BV/TV ($R = -0.67$). These results are consistent with a previous study [39] where the authors obtained a moderate positive correlation between bone apparent density with $FIAB_p$ ($R = 0.37$, $n = 22$), and a negative correlation with $FSAB_p$ ($R = -0.69$, $n = 22$), using periodogram at 1.0 MHz. However, the AR-FIAB have much higher correlations with BV/TV ($R_{Burg} = 0.88$, $R_{cov} = 0.89$, $R_{mcov} = 0.88$, $n = 26$) than $FIAB_p$ ($R = 0.71$, $n = 26$), and the AR-FSAB obtained more negative Pearson's R coefficients with BV/TV ($R_{Burg} = -0.84$, $R_{cov} = -0.85$, $R_{mcov} = -0.83$, $n = 26$) than $FSAB_p$ ($R = -0.67$, $n = 26$) in the present study. Since AIB and FIAB have a strong positive correlation with BV/TV as shown in Table 3, we recommend choosing $T1 = 0 - 3.0\ \mu s$ and $T2 = 3.0 - 10.0\ \mu s$ for the SOI to compute AIB and FIAB. For AIB, this is consistent with the pioneering study by Liu *et al.* at [50]. For SCS and FSAB, we recommend T1 and T2 be chosen with the ranges 5.5-10.0 μs for the SOI.

Finally, the one-way ANOVA test results have shown that the AR-based methods are significantly different from the periodogram at least for $p < 0.05$ (Table 2).

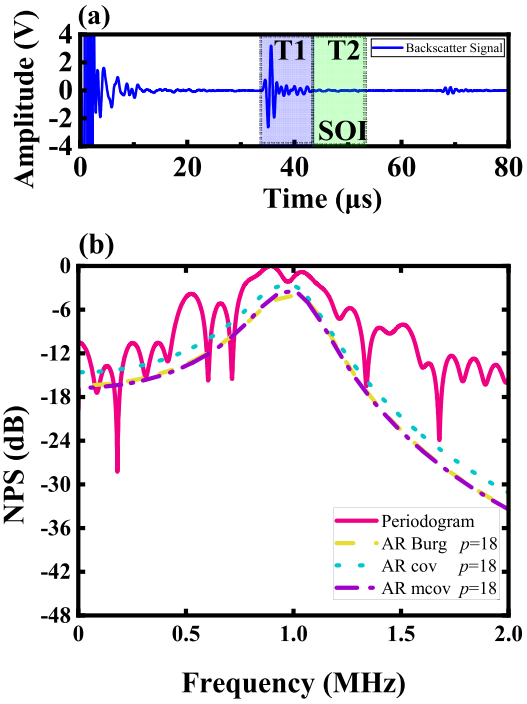

FIGURE 5. (a) The backscatter signal, (b) Normalized power spectrum (NPS) of the backscatter signal.

B. THE EFFECT OF SOI AND SPECTRAL ESTIMATION TO PARAMETERS

Here we present a backscatter signal and its power spectra show in Fig. 5(a). and Fig. 5(b). as an example. The backscatter signal has a 10.0 μs for T1 and 10.0 μs for T2 respectively.

Previous studies have reported that the four backscatter parameters under investigation correlated with the bone parameters, both for *in vitro* and *in vivo* experiments [36], [43], [50]. These parameters require the spectral estimation for extracting features from the backscatter signals. For example, AIB, FIAB, and FSAB were derived from the apparent backscatter transfer function (ABTF). The ABTF is described by the ratio of the power spectral density in (6) [40], which is a product of the backscatter coefficient ($[B(f)]$), the frequency-dependent attenuation ($[A(f)]$), the reflection losses and transmission coefficient ($[R]$), and the diffraction effects ($[D(f)]$):

$$\frac{P_{SOI}(f)}{P_{Ref}(f)} = [B(f)] \cdot [A(f)]^{-1} \cdot [R] \cdot [D(f)]. \quad (6)$$

The attenuation in a scattered media is considered the result of both the scattering and the absorption [57]. The term $[A(f)]$ in (6) might explain a physical reason that correlation changed when increasing the delay time T1. AIB and FIAB are the comprehensive results of ultrasonic backscattering and attenuation effect. When the length of T1 selected short, the backscatter was comparatively strong than attenuation, causing positive correlation with BV/TV at short T1 and negative correlations with increasing T1. SCS and FSAB are mainly due to the frequency-dependent attenuation of

ultrasound in cancellous bone [58]. When T1 is increasing, the backscatter signal at higher frequencies attenuated more than the signals at lower frequencies became pronounced. Thus, correlations between SCS, FSAB and BV/TV were fluctuant when T1 was short, the negative correlations were observed at longer T1 ($5.5\,\mu s < T1 < 10\,\mu s$).

The spectral estimation algorithm was usually chosen based on the investigator's preference. However, the periodogram is not a consistent estimator of the power spectrum [59]–[61]. It is biased toward the true spectrum and exhibits fluctuations. With a rectangular window, the bias can be estimated by

$$Bias\left[\hat{P}(\omega)\right] = \frac{P(\omega)}{N}\left|\left[\frac{\sin\left(\frac{\omega N}{2}\right)}{\sin\left(\frac{\omega}{2}\right)}\right]e^{\frac{-j\omega(N-1)}{2}}\right|^2 - P(\omega). \quad (7)$$

Given a finite length T2 with sample points N, the estimated spectrum $\hat{P}(\omega)$ is biased to the true spectrum $P(\omega)$. When T2 increases toward infinity, the periodogram is asymptotically unbiased. However, when T2 increases, the variance does not tend to zero in the covariance [62] expression as:

$$\lim_{N\to\infty} Var\left[\hat{P}(\omega)\right] = \lim_{N\to\infty} P^2(\omega)\left\{1+\left[\frac{\sin(\omega N)}{N\,.\,\sin(\omega)}\right]^2\right\} \neq 0. \quad (8)$$

Moreover, the strong attenuation of ultrasound in the cancellous bone will yield SOI with a poor signal-to-noise ratio (i.e., the range between 54.35 μs to 68.70 μs) as shown in Fig. 5(a). The signal after 68.70 μs should be excluded because it is the multiple reflections between the surface of cancellous bone and the transducer. Thus, we choose the ranges 0-10.0 μs and 1.0-10.0 μs for respective T1 and T2 for analysis in this study. The periodogram only used the finite length T2 to estimate spectrum is one of a cause of backscatter parameters fluctuations. The periodogram power spectra generate large variances and fluctuations, as shown in Fig. 5(b). The AR-based power spectrum minimizes the prediction error and estimates the spectrum more stable and look very similar with small variance. Since the computation of the ultrasonic parameters requires the power spectral density estimation, the AR-algorithms have overcome these shortcomings of the classical spectral method. It might be a reason that the AR-based ultrasound parameters have higher correlation with BV/TV.

C. SELECTING P-ORDER FOR AR MODEL

Selecting a proper order p is essential in an AR model for the power spectral density estimation. An inappropriate order will result in inaccuracy and statistical instability. Selecting a too-low order might over-smooth the spectrum. Conversely, a too-large order might create spurious spectral peaks. It was suggested that the p-order should be between N/3 and N/2 where N is the number of data points [63]. In this study, the shortest T2 was set at 1.0 μs with a 50 MHz sampling frequency; the N value was at least 50. To study the effect of AR order p on the power spectral estimation,

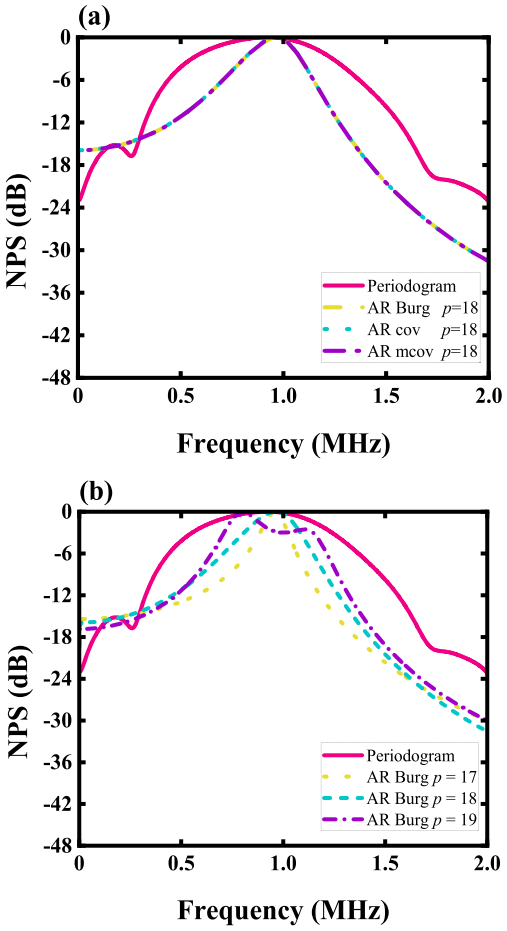

FIGURE 6. Normalized power spectrum (NPS) of the reference signal: (a) Periodogram and three AR algorithms with order $p = 18$ estimated, (b) Periodogram and AR Burg algorithm with the different p-order estimated.

we examined the power spectrum of the reference signal using AR estimation with orders from 17 to 25. The spectrum has insufficient frequency resolution to reflect the true spectrum when $p \leq 16$. However, when $p \geq 19$, it resulted in spurious peaks and serious estimation as shown in Fig. 6(b).

Similar results can also be observed for AR cov and AR mcov. To seek for an appropriate p-order within the interval of [N/3, N/2], a large p-order may render a more accurate estimation of the power spectrum; however, spurious peaks and computation cost will also increase. Therefore, the choice of order p should take a balance between the computation cost and the accuracy of the spectral estimation. Finally, we chose p-order of 17 and 18 for estimators.

D. LIMITATIONS

This study involves the measurements performed on the bovine cancellous bones *in vitro*, which required the infilled marrow to be removed. Before CT-scanning, removing the cortical bone by cutting and the marrow by high-pressure water cleaning might damage some trabeculae and thus change the microstructures. This should be considered

when the microstructure-related parameters are analyzed. AR-based parameters may not be directly used *in vivo* measurement, both the soft tissue and the curved cortical bone may become sources of error. Thus, the selection of ROI, SOI and AR p-order should be carefully studied *in vivo*. Although BV/TV is one of the critical parameters to assess cancellous bones, previous studies have also reported the bone microstructures parameters, such as trabecular thickness, trabecular spacing, and porosity, have significant correlations with the ultrasonic backscatter parameters [64]–[67]. The correlations of these bone parameters with ultrasonic backscatter parameters were not addressed in this study and will be carried out in our future work.

V. CONCLUSIONS

The correlations between ultrasonic backscatter parameters and BV/TV were studied using four spectral estimators. The main findings of the present study are the following. (1) The ultrasonic backscatter parameters demonstrate significantly strong correlations with BV/TV. (2) The spectral estimation algorithms affected the estimated values of ultrasonic backscatter parameters and the subsequent correlation strength with BV/TV for cancellous bone evaluation. (3) The periodogram is not a good spectral estimator. Selecting the appropriate AR p-order and SOI, the AR-optimized parameters exhibit stronger correlations with BV/TV than using the periodogram method. These results indicate that the AR-based method has a promising potential to enhance the performance of evaluation and diagnosis of cancellous bone using ultrasonic backscatter method.

APPENDIX

A. AR BURG ESTIMATOR

AR Burg estimator is based on the minimization of the forward and backward prediction error [68] and estimation of the AR coefficients, $a_1, a_2, a_k, \ldots, a_p$, and is defined by

$$\begin{cases} \hat{e}_p^f[n] = x[n] + \sum_{k=1}^{p} \hat{a}_{p,k} x[n-k], \\ \qquad n = p+1, \ldots, N \\ \hat{e}_p^b[n] = x[n-p] + \sum_{k=1}^{p} \hat{a}_{p,k}^* x[n-k], \\ \qquad n = p+1, \ldots, N \end{cases} \tag{A.1}$$

where the superscript "$\boldsymbol{f}$" and "$\boldsymbol{b}$" denote the forward and backward prediction, respectively. The AR coefficients are related to the reflection coefficient $\hat{K}_p$ by

$$\hat{a}_{p-1,k} = \begin{cases} \hat{a}_{p-1,k} + \hat{K}_p \hat{a}_{p-1,p-k}^*, & k = 1, \ldots, p-1, \\ \hat{K}_p, & k = p. \end{cases} \tag{A.2}$$

where the symbol "$*$" denotes the complex conjugate [69]. Then the reflection coefficients $\hat{K}_p$ are defined by

$$\hat{K}_p = \frac{-\sum_{p+1}^{N} \hat{e}_{p-1}^f[n]\, \hat{e}_{p-1}^{*b}[n-1]}{\frac{1}{2}\sum_{p+1}^{N} \left[\left| \hat{e}_{p-1}^f[n] \right|^2 + \left| \hat{e}_{p-1}^b[n-1] \right|^2 \right]}. \tag{A.3}$$

The prediction errors satisfy the following recursive-in-order expressions

$$\begin{cases} \hat{e}_p^f[n] = \hat{e}_{p-1}^f[n] + \hat{K}_p \hat{e}_{p-1}^b[n-1] \\ \hat{e}_p^b[n] = \hat{e}_{p-1}^b[n-1] + \hat{K}_p^* \hat{e}_{p-1}^f[n] \end{cases} \tag{A.4}$$

The total least squares error is defined as

$$\hat{e}_{min} = \hat{e}_{p-1}^f[n] + \hat{K}_p \hat{e}_{p-1}^b[n-1] + \hat{e}_{p-1}^b[n-1] + \hat{K}_p^* \hat{e}_{p-1}^f[n]. \tag{A.5}$$

Based on the estimates of the AR coefficients, the power spectral density estimation is [70] as

$$\hat{P}_{Burg}(f) = \frac{\hat{e}_{min}}{\left| 1 + \sum_{k=1}^{P} \hat{a}_{p,k} e^{-(j2\pi kf)} \right|^2}. \tag{A.6}$$

B. AR COVARIANCE ESTIMATOR

The AR Covariance estimator minimizes the forward prediction error as:

$$\hat{e} = \frac{1}{N-p} \sum_{n=p}^{N-1} \left| x[n] + \sum_{k=1}^{p} a_k x[n-k] \right|^2. \tag{A.7}$$

The solution of the equations can be written:

$$\begin{bmatrix} \hat{c}(1,0) \\ \hat{c}(2,0) \\ \vdots \\ \hat{c}(p,0) \end{bmatrix} + \begin{bmatrix} \hat{c}(1,1) & \hat{c}(1,2) & \cdots & \hat{c}(1,p) \\ \hat{c}(2,1) & \hat{c}(2,2) & \vdots & \hat{c}(2,p) \\ \vdots & \vdots & \ddots & \vdots \\ \hat{c}(p,1) & \hat{c}(p,2) & \cdots & \hat{c}(p,p) \end{bmatrix} \begin{bmatrix} \hat{a}(1) \\ \hat{a}(2) \\ \vdots \\ \hat{a}(p) \end{bmatrix} = \begin{bmatrix} 0 \\ 0 \\ \vdots \\ 0 \end{bmatrix} \tag{A.8}$$

where

$$\hat{c}(j,k) = \frac{1}{N-p} \sum_{n=p}^{N-1} x^*[n-j] x[n-k], \quad j, \quad k = 0, 1, \ldots, p \tag{A.9}$$

The AR coefficients can be calculated by

$$\begin{bmatrix} \hat{a}(1) \\ \hat{a}(2) \\ \vdots \\ \hat{a}(p) \end{bmatrix} = - \begin{bmatrix} \hat{c}(1,1) & \hat{c}(1,2) & \cdots & \hat{c}(1,p) \\ \hat{c}(2,1) & \hat{c}(2,2) & \vdots & \hat{c}(2,p) \\ \vdots & \vdots & \ddots & \vdots \\ \hat{c}(p,1) & \hat{c}(p,2) & \cdots & \hat{c}(p,p) \end{bmatrix}^{-1} \times \begin{bmatrix} \hat{c}(1,0) \\ \hat{c}(2,0) \\ \vdots \\ \hat{c}(p,0) \end{bmatrix} \tag{A.10}$$

With the white noise variance $\hat{\sigma}^2$ estimated by

$$\hat{\sigma}^2 = \hat{e}_{min} = c(0,0) + \sum_{k=1}^{P} \hat{a}_k c(0,k). \tag{A.11}$$

Then, the power spectral estimation is [71]

$$\hat{P}_{cov}(f) = \frac{\hat{e}_{min}}{\left| 1 + \sum_{k=1}^{P} \hat{a}_k e^{-(j2\pi kf)} \right|^2}. \tag{A.12}$$

C. AR MODIFIED COVARIANCE ESTIMATOR

The AR modified covariance estimator minimizes the forward and backward prediction errors. For an AR(p) process the optimal forward predictor and the optimal backward predictor are described by

$$\begin{cases} \hat{x}^f[n] = -\sum_{k=1}^{p} a_k x[n-k], \\ \hat{x}^b[n] = -\sum_{k=1}^{p} a_k^* x[n+k]. \end{cases} \tag{A.13}$$

The estimated forward and backward prediction error powers can be written

$$\begin{cases} \hat{e}^f = \frac{1}{N-p}\sum_{n=p}^{N-1}\left|x[n] + \sum_{k=1}^{p} a_k x[n-k]\right|^2, \\ \hat{e}^b = \frac{1}{N-p}\sum_{n=0}^{N-1-p}\left|x[n] + \sum_{k=1}^{p} a_k^* x[n+k]\right|^2. \end{cases} \tag{A.14}$$

The AR Modified covariance minimizes the average of the estimated forward and backward prediction error powers as

$$\hat{e}_{min} = \frac{\left(\hat{e}^f + \hat{e}^b\right)}{2}. \tag{A.15}$$

The AR coefficients can be computed by (A10) with the definition of $\hat{c}(\mathbf{j}, \mathbf{k})$ replaced by

$$\begin{aligned} \hat{c}(j,k) = \frac{1}{2(N-p)}\Bigg[&\sum_{n=p}^{N-1} x^*[n-j]x[n-k] \\ &+ \sum_{n=0}^{N-1-p} x[n+j]x^*[n+k]\Bigg], \\ j, \quad k = 1, 2, \ldots, p. \end{aligned} \tag{A.16}$$

With the white noise variance $\hat{\sigma}^2$ estimated by

$$\begin{aligned} &\hat{\sigma}^2 \\ &= \hat{e}_{min} = \frac{1}{2(N-p)}\left\{\sum_{n=p}^{N-1}\left(x[n] + \sum_{k=1}^{P}\hat{a}_k\right)x^*[n]\right. \\ &\left. + \sum_{n=0}^{N-1-p}\left(x^*[n] + \sum_{k=1}^{P}\hat{a}_k x^*[n+k]\right)x[n]\right\}. \end{aligned} \tag{A.17}$$

Then, the power spectral density estimation is [72]

$$\hat{P}_{mcov}(f) = \frac{\hat{e}_{min}}{\left|1 + \sum_{k=1}^{P}\hat{a}_k e^{-(j2\pi kf)}\right|^2}. \tag{A.18}$$

ACKNOWLEDGMENT

Lawrence H. Le is a Senior Visiting Scholar at the State Key Laboratory of ASIC and System of Fudan University for the joint work.

REFERENCES

[1] C. H. Wu, S. T. Tu, Y. F. Chang, D. C. Chan, J. T. Chien, C. H. Lin, and K. S. Tsai, "Fracture liaison services improve outcomes of patients with osteoporosis-related fractures: A systematic literature review and meta-analysis," *Bone*, vol. 111, pp. 92–100, Jun. 2018.

[2] M. P. Høiberg, K. H. Rubin, A. P. Hermann, K. Brixen, and B. Abrahamsen, "Diagnostic devices for osteoporosis in the general population: A systematic review," *Bone*, vol. 92, pp. 58–69, Nov. 2016.

[3] T. D. Rachner, S. Khosla, and L. C. Hofbauer, "Osteoporosis: Now and the future," *Lancet*, vol. 377, no. 9773, pp. 1276–1287, 2011.

[4] D. Kendler, "Osteoporosis: Therapies now and in the future," *Climacteric*, vol. 14, no. 5, pp. 604–605, Oct. 2011.

[5] T. Rolvien, J. Stürznickel, F. N. Schmidt, S. Butscheidt, T. Schmidt, B. Busse, S. Mundlos, T. Schinke, U. Kornak, M. Amling, and R. Oheim, "Comparison of bone microarchitecture between adult osteogenesis imperfecta and early-onset osteoporosis," *Calcified Tissue Int.*, vol. 103, no. 5, pp. 512–521, Nov. 2018.

[6] P. G. Trafton, "Fragility fractures in the developing world: A rising challenge," *Current Geriatrics Rep.*, vol. 7, no. 4, pp. 278–287, Dec. 2018.

[7] S. Yedavally-Yellayi, A. M. Ho, and E. M. Patalinghug, "Update on Osteoporosis," *Primary Care*, vol. 46, no. 1, p. 175, Mar. 2019.

[8] A. Oden, E. V. McCloskey, J. A. Kanis, N. C. Harvey, and H. Johansson, "Burden of high fracture probability worldwide: Secular increases 2010–2040," *Osteoporosis Int.*, vol. 26, no. 9, pp. 2243–2248, Sep. 2015.

[9] A. J. Rodriguez, H. A. Fink, L. Mirigian, N. Guañabens, R. Eastell, K. Akesson, and P. R. Ebeling, "Pain, quality of life, and safety outcomes of kyphoplasty for vertebral compression fractures: Report of a task force of the american society for bone and mineral research," *J. Bone Mineral Res.*, vol. 32, no. 9, pp. 1935–1944, Sep. 2017.

[10] B. L. Riggs and L. J. Melton, "The worldwide problem of osteoporosis: Insights afforded by epidemiology," *Bone*, vol. 17, no. 5, pp. S505–S511, Nov. 1995.

[11] J. Magaziner, W. Hawkes, J. R. Hebel, S. I. Zimmerman, K. M. Fox, M. Dolan, G. Felsenthal, and J. Kenzora, "Recovery from hip fracture in eight areas of function," *J. Gerontol. Ser. A-Biol. Sci. Med. Sci.*, vol. 55, no. 9, pp. M498–M507, Sep. 2000.

[12] C. Cooper, "The crippling consequences of fractures and their impact on quality of life," *Amer. J. Med.*, vol. 103, no. 2, pp. 12–19, Aug. 1997.

[13] S. Williamson, F. Landeiro, T. McConnell, L. Fulford-Smith, M. K. Javaid, A. Judge, and J. Leal, "Costs of fragility hip fractures globally: A systematic review and meta-regression analysis," *Osteoporosis Int.*, vol. 28, no. 10, pp. 2791–2800, Oct. 2017.

[14] M. A. M. Althomali, M.-L. Wille, M. P. Shortell, and C. M. Langton, "Estimation of mechanical stiffness by finite element analysis of ultrasound computed tomography (UCT-FEA); A comparison with X-ray μCT based FEA in cancellous bone replica models," *Appl. Acoust.*, vol. 133, pp. 8–15, Apr. 2018.

[15] A. H. Alomari, M.-L. Wille, and C. M. Langton, "Bone volume fraction and structural parameters for estimation of mechanical stiffness and failure load of human cancellous bone samples; in-vitro comparison of ultrasound transit time spectroscopy and X-ray μCT," *Bone*, vol. 107, pp. 145–153, Feb. 2018.

[16] P. Martineau, B. C. Silva, and W. D. Leslie, "Utility of trabecular bone score in the evaluation of osteoporosis," *Current Opinion Endocrinol. Diabetes Obesity*, vol. 24, no. 6, pp. 402–410, Dec. 2017.

[17] X. Qu, Z. Yu, X. Liu, and T. Tang, "The effect of ageing and osteoarthritis on the mechanical properties of cartilage and bone in the human knee joint," *J. Bone Mineral Res.*, vol. 32, pp. S141–S142, Dec. 2017.

[18] L. Gennari, S. Rotatori, S. Bianciardi, R. Nuti, and D. Merlotti, "Treatment needs and current options for postmenopausal osteoporosis," *Expert Opinion Pharmacotherapy*, vol. 17, no. 8, pp. 1141–1152, May 2016.

[19] J. S. Chen, J. M. Simpson, F. Blyth, and L. M. March, "Managing osteoporosis with FRAX in Australia: Proposed new treatment thresholds from the 45&Up Study cohort," *Osteoporosis Int.*, vol. 24, pp. 148–153, Dec. 2013.

[20] Y.-C. Lu, Y. C. Lin, Y. K. Lin, Y. J. Liu, K. H. Chang, P. U. Chieng, and W. P. Chan, "Prevalence of osteoporosis and low bone mass in older chinese population based on bone mineral density at multiple skeletal sites," *Sci. Rep.*, vol. 6, May 2016, Art. no. 25206.

[21] K. Harrar, L. Hamami, E. Lespessailles, and R. Jennane, "Piecewise Whittle estimator for trabecular bone radiograph characterization," *Biomed. Signal Process. Control*, vol. 8, no. 6, pp. 657–666, Nov. 2013.

[22] V. C. Korfiatis, S. Tassani, and G. K. Matsopoulos, "A new ensemble classification system for fracture zone prediction using imbalanced micro-CT bone morphometrical data," *IEEE J. Biomed. Health Inform.*, vol. 22, no. 4, pp. 1189–1196, Jul. 2018.

[23] P. Fratzl, H. S. Gupta, E. P. Paschalis, and P. Roschger, "Structure and mechanical quality of the collagen-mineral NANO-composite in bone," *J. Mater. Chem.*, vol. 14, no. 14, pp. 2115–2123, 2004.

[24] Q. Grimal and P. Laugier, "Quantitative ultrasound assessment of cortical bone properties beyond bone mineral density," *IRBM*, vol. 40, no. 1, pp. 16–24, Feb. 2019.

[25] R. T. Ribeiro, R. T. Marinho, and J. M. Sanches, "An ultrasound-based computer-aided diagnosis tool for steatosis detection," *IEEE J. Biomed. Health Informat.*, vol. 18, no. 4, pp. 1397–1403, Jul. 2014.

[26] M. Hajian, R. Gaspar, and R. G. Maev, "Accurate 3-D profile extraction of skull bone using an ultrasound matrix array," *IEEE Trans. Biomed. Eng.*, vol. 64, no. 12, pp. 2858–2871, Dec. 2017.

[27] D. Hans and S. Baim, "Quantitative ultrasound (QUS) in the management of osteoporosis and assessment of fracture risk," *J. Clin. Densitometry*, vol. 20, no. 3, pp. 322–333, Jul. 2017.

[28] M.-A. Krieg, R. Barkmann, S. Gonnelli, A. Stewart, D. C. Bauer, L. D. R. Barquero, J. J. Kaufman, R. Lorenc, P. D. Miller, W. P. Olszynski, C. Poiana, A.-M. Schott, E. M. Lewiecki, and D. Hans, "Quantitative ultrasound in the management of osteoporosis: The 2007 ISCD official positions," *J. Clin. Densitometry*, vol. 11, no. 1, pp. 163–187, Jan. 2008.

[29] K. A. Wear, S. Nagaraja, M. L. Dreher, S. Sadoughi, S. Zhu, and T. M. Keaveny, "Relationships among ultrasonic and mechanical properties of cancellous bone in human calcaneus *in vitro*," *Bone*, vol. 103, pp. 93–101, Oct. 2017.

[30] K. Yoon, W. Lee, P. Croce, A. Cammalleri, and S.-S. Yoo, "Multi-resolution simulation of focused ultrasound propagation through ovine skull from a single-element transducer," *Phys. Med. Biol.*, vol. 63, no. 10, May 2018, Art. no. 105001.

[31] T. De Marco, M. Peccarisi, F. Conversano, A. Greco, S. Chiozzi, F. De Pascalis, and S. Casciaro, "A new approach for measuring the trabecular bone density through the echosound backscattering: An ex vivo validation on human femoral heads," *Meas.*, vol. 87, pp. 51–61, Jun. 2016.

[32] S. Pichardo, V. W. Sin, and K. Hynynen, "Multi-frequency characterization of the speed of sound and attenuation coefficient for longitudinal transmission of freshly excised human skulls," *Phys. Med. Biol.*, vol. 56, no. 1, pp. 219–250, Jan. 2011.

[33] B. S. Garra, M. Locher, S. Felker, and K. A. Wear, "Measurements of ultrasonic backscattered spectral centroid shift from spine *In Vivo*: Methodology and preliminary results," *Ultrasound Med. Biol.*, vol. 35, no. 1, pp. 165–168, Jan. 2009.

[34] J. P. Karjalainen, J. Töyräs, O. Riekkinen, M. Hakulinen, and J. S. Jurvelin, "Ultrasound backscatter imaging provides frequency-dependent information on structure, composition and mechanical properties of human trabecular bone," *Ultrasound Med. Biol.*, vol. 35, no. 8, pp. 1376–1384, Aug. 2009.

[35] K. A. Wear, "Ultrasonic scattering from cancellous bone: A review," *IEEE Trans. Ultrason., Ferroelectr., Freq. Control*, vol. 55, no. 7, pp. 1432–1441, Jul. 2008.

[36] D. Ta, W. Wang, K. Huang, Y. Wang, and L. H. Le, "Analysis of frequency dependence of ultrasonic backscatter coefficient in cancellous bone," *J. Acoust. Soc. America*, vol. 124, no. 6, pp. 4083–4090, Dec. 2008.

[37] K. A. Wear, B. S. Garra, M. C. Pinet, S. Felker, and J. Mai, "Measurements of ultrasonic backscattered spectral centroid shift from spine *In Vivo*: Methodology and preliminary results," *Ultrasound Med. Biol.*, vol. 17, pp. 165–168, Sep. 2002.

[38] B. K. Hoffmeister, D. P. Johnson, J. A. Janeski, D. A. Keedy, B. W. Steinert, A. M. Viano, and S. C. Kaste, "Ultrasonic characterization of human cancellous bone *in vitro* using three different apparent backscatter parameters in the frequency range 0.6-15.0 mhz," *IEEE Trans. Ultrason., Ferroelectr., Freq. Control*, vol. 55, no. 7, pp. 52–1442, Jul. 2008.

[39] B. K. Hoffmeister, "Frequency dependence of apparent ultrasonic backscatter from human cancellous bone," *Phys. Med. Biol.*, vol. 56, no. 3, pp. 83–667, Feb. 2011.

[40] B. K. Hoffmeister, J. A. McPherson, M. R. Smathers, P. L. Spinolo, and M. E. Sellers, "Ultrasonic backscatter from cancellous bone: The apparent backscatter transfer function," *IEEE Trans. Ultrason., Ferroelectr., Freq. Control*, vol. 62, no. 12, pp. 2115–2125, Dec. 2015.

[41] B. K. Hoffmeister, P. L. Spinolo, M. E. Sellers, P. L. Marshall, A. M. Viano, and S. R. Lee, "Effect of intervening tissues on ultrasonic backscatter measurements of bone: An *in vitro* study," *J. Acoust. Soc. Amer.*, vol. 138, no. 4, pp. 2449–2457, Oct. 2015.

[42] B. K. Hoffmeister, M. R. Smathers, C. J. Miller, J. A. McPherson, C. R. Thurston, P. L. Spinolo, and S. R. Lee, "Backscatter-difference measurements of cancellous bone using an ultrasonic imaging system," *Ultrasonic Imag.*, vol. 38, no. 4, pp. 285–297, Jul. 2016.

[43] Y. Q. Jiang, C.-H. Liu, R.-Y. Li, W.-P. Wang, H. Ding, Q. Qi, D. Ta, J. Dong, and W.-Q. Wang, "Analysis of apparent integrated backscatter coefficient and backscattered spectral centroid shift in calcaneus *In Vivo* for the ultrasonic evaluation of osteoporosis," *Ultrasound Med. Biol.*, vol. 40, no. 6, pp. 17–1307, Jun. 2014.

[44] D. Ta, K. Huang, and W. Wang, "Correlations between signal spectrum of ultrasonic backscatter and cancellous bone microstructure," in *Proc. IEEE Int. Ultrason. Symp.*, Sep. 2009, pp. 1–4.

[45] B. K. Hoffmeister, A. M. Viano, L. C. Fairbanks, S. C. Ebron, J. A. McPherson, and M. T. Huber, "Effect of gate choice on backscatter difference measurements of cancellous bone," *J. Acoust. Soc. Amer.*, vol. 142, no. 2, pp. 540–550, Aug. 2017.

[46] B. K. Hoffmeister, M. T. Huber, A. M. Viano, and J. S. Huang, "Characterization of a polymer, open-cell rigid foam that simulates the ultrasonic properties of cancellous bone," *J. Acoust. Soc. Amer.*, vol. 143, no. 2, pp. 911–920, Feb. 2018.

[47] S. M. Alessio, "Parametric spectral methods," in *Digital Signal Processing and Spectral Analysis for Scientists*. Cham, Switzerland: Springer, 2016, pp. 465–535. doi: 10.1007/978-3-319-25468-5.

[48] X. Y. Yang, T. G. Xu, S.-N. Fu, L. Zeng, and X. J. Bian, "Classical and modern power spectrum estimation for tune measurement in CSNS RCS," *Chin. Phys. C*, vol. 37, no. 11, Nov. 2013, Art. no. 117003.

[49] Z. Leonowicz, T. Lobos, and J. Rezmer, "Advanced spectrum estimation methods for signal analysis in power electronics," *IEEE Trans. Ind. Electron.*, vol. 50, no. 3, pp. 514–519, Jun. 2003.

[50] C. Liu, T. Tang, F. Xu, D. Ta, M. Matsukawa, B. Hu, and W. Wang, "Signal of interest selection standard for ultrasonic backscatter in cancellous bone evaluation," *Ultrasound Med. Biol.*, vol. 41, no. 10, pp. 2714–2721, Oct. 2015.

[51] Y. B. Yan, W. Qi, T. X. Qiu, E. C. Teo, and W. Lei, "The effect of threshold value on the architectural parameters and stiffness of human cancellous bone in micro CT analysis," *J. Mech. Med. Biol.*, vol. 12, no. 5, Dec. 2012, Art. no. 1250092.

[52] C. C. Liu, D. A. Ta, F. Fujita, T. Hachiken, M. Matsukawa, K. Mizuno, and W. Q. Wang, "The relationship between ultrasonic backscatter and trabecular anisotropic microstructure in cancellous bone," *J. Appl. Phys.*, vol. 115, no. 6, Feb. 2014, Art. no. 064906 .

[53] Y. Li, B. Li, F. Xu, C. Liu, D. Ta, and W. Wang, "Ultrasonic backscatter measurements at the calcaneus: An *in vivo* study," *Measurement*, vol. 122, pp. 128–134, Jul. 2018.

[54] K. A. Wear, R. F. Wagner, and B. S. Garra, "High resolution ultrasonic backscatter coefficient estimation based on autoregressive spectral estimation using Burg's algorithm," *IEEE Trans. Med. Imag.*, vol. 13, no. 3, pp. 500–507, Sep. 1994.

[55] M. K. Malo, J. Töyräs, J. P. Karjalainen, H. Isaksson, O. Riekkinen, and J. S. Jurvelin, "Ultrasound backscatter measurements of intact human proximal femursâĂŤRelationships of ultrasound parameters with tissue structure and mineral density," *Bone*, vol. 64, pp. 240–245, Jul. 2014.

[56] J. M. Giron-Sierra, "Experimental Modelling," *Digit. Signal Process. Matlab Examples*, vol. 2, pp. 581–645, Jul. 2017.

[57] O. Yousefian, R. D. White, Y. Karbalaeisadegh, H. T. Banks, and M. Müller, "The effect of pore size and density on ultrasonic attenuation in porous structures with mono-disperse random pore distribution: A two-dimensional in-silico study," *J. Acoust. Soc. Amer.*, vol. 144, no. 2, pp. 709–719, Aug. 2018.

[58] C. Liu, B. Li, Q. Diwu, Y. Li, R. Zhang, D. Ta, and W. Wang, "Relationships of ultrasonic backscatter with bone densities and microstructure in bovine cancellous bone," *IEEE Trans. Ultrason., Ferroelectr., Freq. Control*, vol. 65, no. 12, pp. 2311–2321, Dec. 2018.

[59] D. Barrera, "Quenched invariance principles for the discrete Fourier transforms of a stationary process," *Bernoulli*, vol. 24, no. 2, pp. 1307–1350, May 2018.

[60] S. Birr, H. Dette, M. Hallin, T. Kley, and S. Volgushev, "On Wigner–Ville spectra and the uniqueness of time-varying copula-based spectral densities," *J. Time Ser. Anal.*, vol. 39, no. 3, pp. 242–250, May 2018.

[61] S. S. Rao, "Orthogonal samples for estimators in time series," *J. Time Ser. Anal.*, vol. 39, no. 3, pp. 313–337, May 2018.

[62] S. M. Alessio, "Non-parametric spectral methods," in *Digital Signal Processing and Spectral Analysis for Scientists: Concepts and Applications*. Cham, Switzerland: Springer, 2016, pp. 403–464.

[63] T. J. Ulrych and T. N. Bishop, "Maximum entropy spectral analysis and autoregressive decomposition," *Rev. Geophys.*, vol. 13, no. 1, pp. 183–200, Feb. 1975, 1975.

[64] K. I. Lee, "Relationships of linear and nonlinear ultrasound parameters with porosity and trabecular spacing in trabecular-bone-mimicking phantoms," *J. Acoust. Soc. Amer.*, vol. 140, no. 6, pp. EL528–EL533, Dec. 2016.

[65] K. A. Wear, "Nonlinear attenuation and dispersion in human calcaneus *in vitro*: Statistical validation and relationships to microarchitecture," *J. Acoust. Soc. Amer.*, vol. 137, no. 3, pp. 1126–1133, Mar. 2015.
[66] M. A. Hakulinen, J. S. Day, J. Toyras, H. Weinans, and J. S. Jurvelin, "Ultrasonic characterization of human trabecular bone microstructure," *Phys. Med. Biol.*, vol. 51, no. 6, pp. 1633–1648, Mar. 2006.
[67] J. M. Alves, W. Xu, D. Lin, R. S. Siffert, J. T. Ryaby, and J. J. Kaufman, "Ultrasonic assessment of human and bovine trabecular bone: A comparison study," *IEEE Trans. Biomed. Eng.*, vol. 43, no. 3, pp. 249–258, Mar. 1996.
[68] Y. Nam, B. A. Reyes, and K. H. Chon, "Estimation of respiratory rates using the built-in microphone of a smartphone or headset," *IEEE J. Biomed. Health Informat.*, vol. 20, no. 6, pp. 1493–1501, Nov. 2016.
[69] L. Marple, "A new autoregressive spectrum analysis algorithm," *IEEE Trans. Acoust., Speech, Signal Process.*, vol. SMCA-28, no. 4, pp. 441–454, Aug. 1980.
[70] E. D. Übeyli and í. Güler, "Selection of optimal AR spectral estimation method for internal carotid arterial Doppler signals using Cramer–Rao bound," *Comput. Electr. Eng.*, vol. 30, no. 7, pp. 491–508, Oct. 2004.
[71] R. Takalo, H. Hytti, and H. Ihalainen, "Tutorial on univariate autoregressive spectral analysis," *J. Clin. Monit. Comput.*, vol. 19, no. 6, pp. 401–410, Dec. 2005.
[72] A. Subasi, "Selection of optimal AR spectral estimation method for EEG signals using Cramer-Rao bound," *Comput. Biol. Med.*, vol. 37, no. 2, pp. 94–183, Feb. 2007.

BOYI LI was born in Hohhot, China, in 1990. He received the B.S. degree from the Department of Information and Engineering Technology, Sichuan Agricultural University, Ya'an, China, in 2012, and the M.S. degree from the Department of Electronic and Information Engineering, Inner Mongolia University, Hohhot, in 2015. He is currently pursuing the Ph.D. degree in biomedical engineering with the Department of Electronic Engineering, Fudan University, Shanghai, China. His main research interests include biomedical ultrasound, signal processing, and statistical analysis.

FENG XU was born in Nanjing, China, in 1982. He received the B.S. degree from the Department of Electronic Information Science and Technology, Nanjing University of Posts and Telecommunications, in 2005, and the Ph.D. degree from the Department of Electronic Engineering, Fudan University, in 2010, where he is currently a Senior Engineer. His research interests include ultrasonic signal processing and system design.

CHENGCHENG LIU was born in Shandong, China, in 1987. He received the B.S. and Ph.D. degrees from the Department of Electronic Engineering, Fudan University, Shanghai, China, in 2009 and 2014, respectively, where he was a Postdoctoral Researcher, from 2014 to 2016. He is currently an Assistant Professor with the School of Physics Science and Engineering, Institute of Acoustics, Tongji University, Shanghai. His research interests include biomedical ultrasound, ultrasonic signal processing, and ultrasonic imaging.

DAN LI was born in Changzhou, China, in 1982. He received the B.Sc., M.S., and Ph.D. degrees in electrical engineering from Fudan University, Shanghai, China, in 2003, 2006, and 2013, respectively, where he is currently an Associate Professor with the Department of Electronic Engineering. His research interests include ultrasonic signal processing and its application to nondestructive testing.

LAWRENCE H. LE received the M.B.A. degree in finance and technology commercialization and the Ph.D. degree in earth physics from the University of Alberta, Edmonton, Canada. He held a Natural Sciences and Engineering Research Council of Canada (NSERC) Postdoctoral Fellowship at the Schlumberger-Doll Research Laboratory, Ridgefield, CT. He started his medical physics residency training at the Department of Radiology and Diagnostic Imaging (DRDI), University of Alberta, in 1994. He joined the DRDI, University of Alberta, as an Academic Staff, and Capital Health, as a Clinical Medical Physicist, in 2000. He is currently a Clinical Professor leading the Graduate Program at DRDI and the Edmonton Authorized Radiation Protection Agency, Alberta Health Services. He is also a Senior Visiting Scholar with the State Key Laboratory of ASIC and System, Fudan University. He directs the Ultrasonic Bone Tissue Characterization and Imaging Group. He guides his students to use vigorous geophysical techniques to image and study bone tissues. His research interests include imaging, signal, and image processing, simulation, and inversion. He is also a member of The American Association of Physicists in Medicine (AAPM) and The Canadian Organization of Medical Physicists (COMP).

DEAN TA was born in China, in 1972. He received the M.S. degree from the Institute of Acoustics, Shaanxi Normal University, Xi'an, China, in 1999, and the Ph.D. degree from Tongji University, Shanghai, China, in 2002. From 2002 to 2004, he was a Postdoctoral Researcher with the Department of Electronic Engineering, Fudan University, Shanghai, where he is currently a Professor. He has contributed over 200 papers and coauthored one book and five patents. His research interests include biomedical ultrasound, medical signal processing, diagnosis systems of medical ultrasound, and applications of ultrasonic-guided waves in medicine and nondestructive examination. He is also the Vice President of the Acoustical Society of China (ASC) and the Chairman of the Biomed Ultrasound Speciality of ASC.

WEIQI WANG was born in Shanghai, China, in 1939. He graduated from the Physics Department, Fudan University, Shanghai, in 1961, where he is currently the Executive Professor and the Supervisor of the Ph.D. Program. His research interests include signal processing, medical electronics, biomedical ultrasound, and the development of the ultrasonic diagnosis systems. He was elected as a member of the Chinese Academy of Engineering, in 1999. He was a recipient of the AIUM/WFUMB Pioneer Award, the National Invention Award (second place), and 17 other awards.